Grid Impedance Estimation for Islanding Detection and Adaptive Control of Converters

Abdelhady Ghanem†*, Mohamed Rashed†*, Mark Sumner†, M. A. El-sayes* and I. I. I. Mansy*

† *Department of Electrical and Electronics Engineering, University of Nottingham, Nottingham, UK.*
* *Electrical Engineering Department, Mansoura University, Mansoura, Egypt.*
E-mail: eexatg@nottingham.ac.uk

Abstract

The grid impedance is time varying due to the changing structure of the power system configuration and it can have a considerable influence on the control and stability of grid connected converters. This paper presents an online grid impedance estimation method using the output switching current ripple of a SVPWM based grid connected converter. The proposed impedance estimation method is derived from the discretised system model using two consecutive samples within the switching period. The estimated impedance is used for islanding detection and online current controller parameter adaptation. Theoretical analysis and MATLAB simulation results are presented to verify the proposed method. The effectiveness of the grid impedance estimator is validated using experimental results.

I. Introduction

An increasing number of power electronic converters are being used to connect renewable energy sources to the grid. In recent years real-time grid impedance estimation has been researched to improve controller stability and protection (islanding detection) in these types of converter [1] – [3]. Methods for grid impedance estimation are generally classified as passive (non-invasive) and active (invasive) [4]. Passive methods use the non-characteristic (harmonic) voltage and current measurements inherently present in the system to estimate impedance whilst active methods deliberately create a disturbance in the grid and the impedance is estimated from the grid response: in general good results can be achieved as the injection gives the measurements used for impedance estimation a high signal to noise ratio (SNR). Passive methods are preferred as they do not create additional disturbances in the grid, however the SNR is much lower and the estimate tends to be poorer.

Several active techniques have been reported in recent years. Ciobotaru *et al*. [4] presented an online impedance estimation technique based on periodical variations of active and reactive power (PQ variations) of the grid connected single phase power converter. In [5, 6] a current spike is deliberately injected at the point of common coupling (PCC) by a grid connected converter. Based on the voltage response to this disturbance, the grid impedance value is determined using Fourier transforms. A similar method employing the Continuous Wavelet Transform (CWT) to derive the impedance from transient data is presented in [7]. Asiminoaei

et al. [8] have used a PV inverter to inject a low frequency non-characteristic harmonic current of 75 Hz by adding a harmonic voltage to the voltage reference of the PV inverter. A Discrete Fourier Transform (DFT) amplitude and phase calculation is then performed to calculate the grid impedance at that frequency. In [9] an injection of a high frequency signal comprising one or two voltage harmonic signals is implemented. The single harmonic injection uses a 500 Hz signal and the double harmonic injection uses a 500 Hz and 600 Hz signals. The authors in [10], presented a power network parameter estimation based on stimulations injected through a pulse width modulator, it creates a stimulation signal based on Pseudo Random Binary Sequences (PRBS) which have been used to create harmonic-rich stimulation. Good impedance estimation can be achieved using the aforementioned active methods; however, they suffer from a certain number of problems. These problems are mainly related to the rate and amplitude of the repeated injections which are usually kept high to increase the SNR and adversely increase the total harmonic distortion. In addition, the estimated impedance accuracy depends on the background harmonics.

In [11], a passive grid impedance estimation method based on the inherent switching feature (high frequency harmonics) of the grid-connected power converter is presented. This method achieved fast and accurate impedance estimation. However, the current at the switching frequency is very small, so more considerations for SNR and small current measurement are required. A grid impedance estimation method based on the excitation of the LCL-filter resonance is presented in [12]. The presented technique is based on the fact that the frequency peak due to the resonance is particularly sensitive to the grid impedance change. The limitations of this method are how to excite the system resonance in a controlled way and the high number of calculations can overload the processing platform. In [13], an Extended Kalman Filter (EKF) is used to estimate the time variant grid impedance. The main disadvantage of this method is the complicated tuning processes for the covariance matrices.

Another example of a passive method [14] is an analytical estimation model created in the stationary reference frame to estimate the total inductance seen by a variable switching frequency converter using two consecutive current samples. However, the estimated inductance is sensitive to system resistance.

In this paper, an improved approach to passive impedance estimation is proposed. It uses closed form models for grid inductance and resistance estimation derived from the discretised system model in a rotating reference frame. It uses

two consecutive samples within the switching period of a SVPWM based converter – it could be argued that it is using the PWM itself as an injection signal to obtain the benefit of improved SNR compared to most passive methods. The new inductance estimator is completely independent from the resistance estimator.

This paper is organized as follows. In section II, the system description and control scheme for a grid connected converter are presented. Section III presents the derivation of the inductance and resistance estimation models. MATLAB based simulation results for different scenarios and applications of the estimated inductance are given and discussed in section IV. Experimental results are presented in section V and finally conclusions are discussed.

II.   System Description

A three-phase grid connected converter system is shown in Fig. 1. The power converter is connected to the PCC via an inductive filter. The converter is operated in current control mode with a sensorless approach to grid voltage detection.
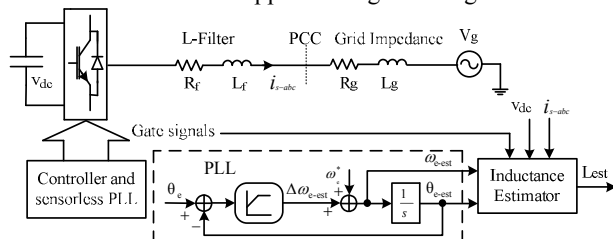

Fig. 1: Three-phase grid connected converter test system.

Current control loop

The current control loop with a sensorless grid voltage detection based on a Phase Locked Loop (PLL) is shown in Fig. 2. The error between the reference and actual measured currents in a *dq* rotating reference frame (synchronised to the grid voltage vector) is processed via a PI controller (together with cross coupling compensation) in order to achieve independent control of active and reactive power and calculate the required converter output reference voltage. A SVPWM technique is used to drive the power converter switches.
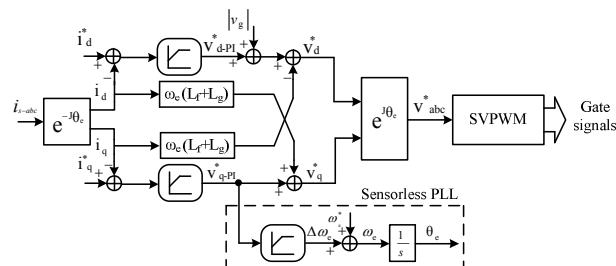

Fig. 2: Current control loop with sensorless PLL.

It should be noted that PLL based synchronisation methods mainly depend on the voltage at the PCC and their dynamic responses adversely affect the overall system stability especially in high impedance networks [15].

In this paper, the grid impedance estimator is based on the current and voltage components measured in the rotating *dq*

reference frame, so it is important to extract the synchronizing angle even if the voltage at PCC is highly polluted due to the presence of a large grid impedance. To overcome this problem, a sensorless grid voltage detection based PLL is used [16]. The output voltage from the PI controller of the quadrature axis current control loop represents the reference quadrature axis component of the grid voltage V_{q-PI}^* and it can be used for synchronization instead of PCC voltage measurement. The PLL is locked by setting V_{q-PI}^* to zero as a phase detector. A PI controller is used to control this component by minimizing the phase error. The output of the PI controller is added to a constant value ω_e^* which represents the nominal frequency and hence the output is the grid voltage frequency ω_e. A Voltage-Controlled Oscillator (VCO), normally an integrator, is then used to extract the grid phase angle θ_e (see Fig. 2).

For the impedance estimator, another slow PLL is used as shown in Fig. 1. The output grid voltage angle from the PLL θ_e is fed to a slow PLL and θ_{e-est} is extracted. θ_{e-est} is used to transform the abc current and voltage to the *dq* rotating reference frame used in impedance estimation only while θ_e is used within the current controller processes and grid synchronization.

Space vector PWM

Fig. 3 shows a representation of the basic space-vector and the reference voltage vector in the stationary reference frame. It can be seen that the grid connected converter shown in Fig. 1 has eight switching states $\vec{V}_1$ to $\vec{V}_8$ where $\vec{V}_1$ to $\vec{V}_6$ are non-zero voltage vectors form the axes of the hexagon and each 60° shift, while $\vec{V}_7$ and $\vec{V}_8$ are zero voltage vectors located at the origin [17]. The objective of the space vector technique is to approximate the reference voltage vector $\vec{V}_c^*$ with the eight space vectors available in VSI. For instance, if $\vec{V}_c^*$ lies between two arbitrary vectors $\vec{V}_i$, $\vec{V}_{i+1}$, only the nearest non-zero vectors ($\vec{V}_i$, $\vec{V}_{i+1}$) and one zero vector ($\vec{V}_7$ or $\vec{V}_8$) should be used. Fig. 4 shows the space vector implementation in sector one as an example.
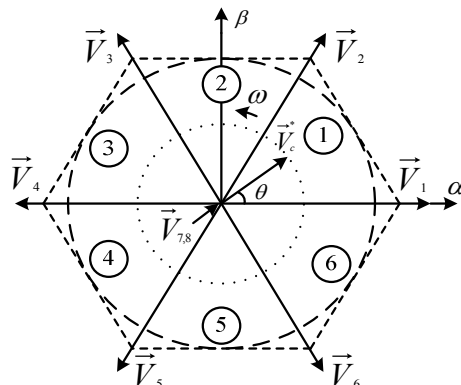

Fig. 3: Basic space vector representation.

The general expressions for each vector time at any sector can be calculated as [17]:

$$T_1 = \frac{\sqrt{3}.T_s.\vec{V}_c^*}{V_{dc}} \sin\left(\frac{\pi}{3} - \theta + \frac{(s_n-1)\pi}{3}\right) \tag{1}$$

2

$$T_2 = \frac{\sqrt{3}.T_s.\vec{V_c^*}}{v_{dc}} \sin\left(\theta - \frac{(s_n-1)\pi}{3}\right) \tag{2}$$

$$T_z = T_s - T_1 - T_2 \tag{3}$$

$$\vec{V_c^*} = \sqrt{(V_{c\alpha}^*)^2 + (V_{c\beta}^*)^2} \quad (4), \qquad \theta = tan^{-1}\left(\frac{V_{c\beta}^*}{V_{c\alpha}^*}\right) \tag{5}$$

Where; T_s is the sampling period, s_n is the sector number which can be determined according to the value of converter reference voltage position.

III. Impedance Estimation Method

The total inductance and resistance (grid plus filter) are estimated using two consecutive current samples measured within the SVPWM period and used with the discretised system model in the rotating dq frame. For the grid connected converter shown in Fig. 1, the continuous-time model in the dq frame is:

$$\frac{d}{dt}i_{dq} = \frac{1}{L}(v_{cdq} - Ri_{dq} - j\omega_e L i_{dq} - v_{gdq}) \tag{6}$$

Where subscript dq denotes the axes of an arbitrary rotating dq frame. c and g refer to converter and grid respectively. Fig. 4 shows typical PWM outputs in sector one and the three fixed measurement instants in each sampling period, which are marked as $k-2$ at the beginning, $k-1$ at $T_s/4$ and k at the middle of the sampling period. It should be noted from Fig. 4 that the converter output phase voltage waveforms are constant during the time intervals of the voltage vectors V_1 and V_2, which e.g. for V_1 are equal to $v_{an}=2V_{dc}/3$, $v_{bn}=-V_{dc}/3$ and $v_{cn}=-V_{dc}/3$. However the equivalent instantaneous dq voltage components during these time intervals are time varying, (see v_d waveform in Fig. 4). Therefore, the discrete form of (6) is given in (7 and 8), where subscript "av" denotes average value, e.g. the discrete voltage v_{cdq-av}^{k-1} is the average value of the instantaneous voltage waveform $v_{cdq}(t)$ over the time interval between the sampling instants $k-1$ and k. The current derivatives in (6) are approximated using the Forward Euler method. The discrete model of (6) for two consecutive samples k and $k-1$ is expressed as:

$$i_{dq}^k = i_{dq}^{k-1} + \frac{T_s}{4L}(v_{cdq-av}^{k-1} - Ri_{dq-av}^{k-1} - j\omega_e i_{dq-av}^{k-1} - v_{gdq-av}^{k-1}) \tag{7}$$

$$i_{dq}^{k-1} = i_{dq}^{k-2} + \frac{T_s}{4L}(v_{cdq-av}^{k-2} - Ri_{dq-av}^{k-2} - j\omega_e i_{dq-av}^{k-2} - v_{gdq-av}^{k-2}) \tag{8}$$

Where;

$$i_{dq-av}^{k-2} = 0.5 \times (i_{dq}^{k-2} + i_{dq}^{k-1}) \tag{9}$$

$$i_{dq-av}^{k-1} = 0.5 \times (i_{dq}^{k-1} + i_{dq}^k) \tag{10}$$

$$v_{cdq-av}^{k-2} = \left(\frac{1}{T_s - T_z}\right)\left[(v_{cdq}^{(1)} + v_{cdq}^{(2)})\frac{T_1}{2} + (v_{cdq}^{(2)} + v_{cdq}^{(3)})\left(\frac{T_s}{4} - \frac{T_z}{4} - \frac{T_1}{2}\right)\right] \tag{11}$$
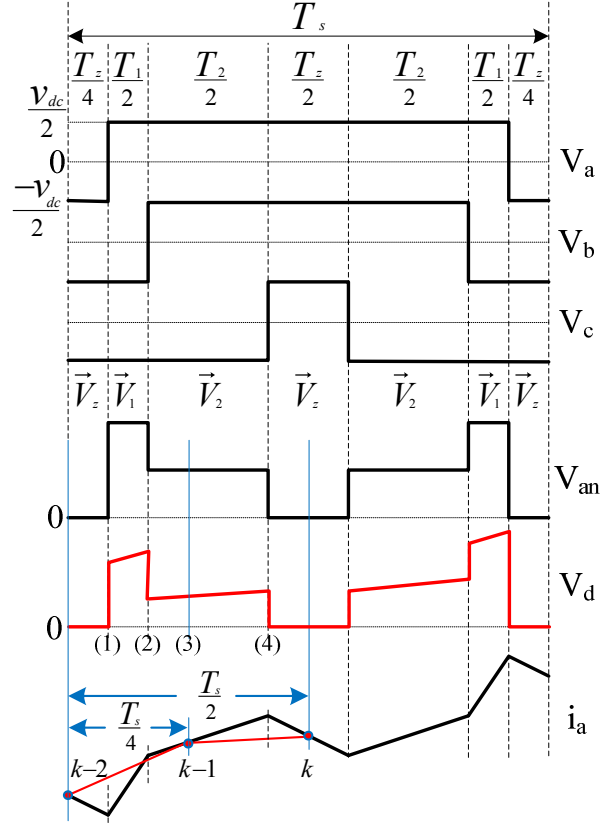

Fig. 4: SVPWM and measuring instants.

$$v_{cdq-av}^{k-1} = 0.5 \times (v_{cdq}^{(3)} + v_{cdq}^{(4)}) \tag{12}$$

The grid voltage is assumed to be slowly varying, so for two consecutive samples, the v_{gdq} components are assumed constant in (7 and 8) and the discrete model can be rearranged as:

$$i_d^k = 2i_d^{k-1} - i_d^{k-2} + \frac{T_s}{4}\left[\frac{1}{L}(v_{cd-av}^{k-1} - v_{cd-av}^{k-2}) - \frac{R}{L}(i_{d-av}^{k-1} - i_{d-av}^{k-2}) + \omega_e(i_{q-av}^{k-1} - i_{q-av}^{k-2})\right] \tag{13}$$

$$i_q^k = 2i_q^{k-1} - i_q^{k-2} + \frac{T_s}{4}\left[\frac{1}{L}(v_{cq-av}^{k-1} - v_{cq-av}^{k-2}) - \frac{R}{L}(i_{q-av}^{k-1} - i_{q-av}^{k-2}) - \omega_e(i_{d-av}^{k-1} - i_{d-av}^{k-2})\right] \tag{14}$$

The discrete models of the two consecutive samples given in (13 and 14) are analytically solved for the unknown parameters $(1/L)$ and (R/L) where R and L are the total resistance and inductance of the system.

$$\frac{1}{L} = \frac{\frac{4}{T_s}\left[(i_d^k-i_d^{k-1})(i_{q-av}^{k-1}-i_{q-av}^{k-2}) - (i_q^k-i_q^{k-1})(i_{d-av}^{k-1}-i_{d-av}^{k-2}) - (i_d^{k-1}-i_d^{k-2})(i_{q-av}^{k-1}-i_{q-av}^{k-2}) + (i_q^{k-1}-i_q^{k-2})(i_{d-av}^{k-1}-i_{d-av}^{k-2})\right] - \omega_e\left[(i_{q-av}^{k-1}-i_{q-av}^{k-2})^2 + (i_{d-av}^{k-1}-i_{d-av}^{k-2})^2\right]}{(v_{cd-av}^{k-1}-v_{cd-av}^{k-2})(i_{q-av}^{k-1}-i_{q-av}^{k-2}) - (v_{cq-av}^{k-1}-v_{cq-av}^{k-2})(i_{d-av}^{k-1}-i_{d-av}^{k-2})} \tag{15}$$

$$\frac{R}{L} = \frac{\frac{4}{T_s}\left[(i_d^k-i_d^{k-1})(v_{cq-av}^{k-1}-v_{cq-av}^{k-2}) - (i_q^k-i_q^{k-1})(v_{cd-av}^{k-1}-v_{cd-av}^{k-2}) - (i_d^{k-1}-i_d^{k-2})(v_{cq-av}^{k-1}-v_{cq-av}^{k-2}) + (i_q^{k-1}-i_q^{k-2})(v_{cd-av}^{k-1}-v_{cd-av}^{k-2})\right] - \omega_e\left[(i_{q-av}^{k-1}-i_{q-av}^{k-2})(v_{cq-av}^{k-1}-v_{cq-av}^{k-2}) + (i_{d-av}^{k-1}-i_{d-av}^{k-2})(v_{cd-av}^{k-1}-v_{cd-av}^{k-2})\right]}{(v_{cd-av}^{k-1}-v_{cd-av}^{k-2})(i_{q-av}^{k-1}-i_{q-av}^{k-2}) - (v_{cq-av}^{k-1}-v_{cq-av}^{k-2})(i_{d-av}^{k-1}-i_{d-av}^{k-2})} \tag{16}$$

After some algebraic manipulation, the solution for the unknown (I/L) and (R/L) are given by (15, 16) as shown at the bottom of the previous page. It is worth noting that the derived inductance and resistance estimator models are fully decoupled and independent.

It should be noted that the (R/L) estimator given by (16) is mainly dependent on the voltage difference and current derivatives between two consecutive samples. It means there is a high sensitivity to inaccurate measurements and averaging which will eventually lead to inaccurate estimates. Therefore, in the following sections only the inductance estimator is investigated.

An important practical issue that affects the accuracy of current measurement during the switching period is the high frequency current ringing that happens after turn on/off switching instants [18] due to parasitic inductances and capacitances within the power electronic system. In order to mitigate this problem, the estimation is disabled if the on/off instants have occurred less than 5 μs before the measuring instants (to allow the ringing to decay).

IV. Simulation Results

The grid connected converter shown in Fig. 1 has been modelled in MATLAB using parameters listed in table (I). A random white Gaussian noise was added to the measured current to reflect realistic measurement noise and the inductance estimation (15) is performed alongside the simulation.

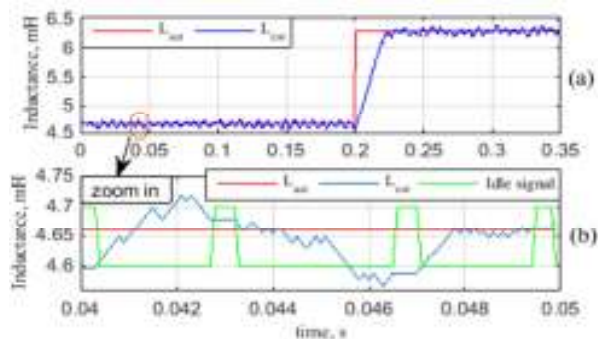| symbol	meaning	value
R_f	Filter Resistance	0.12 Ω
L_f	Filter inductance	4.3 mH
R_g	Grid Resistance	0.113 Ω
L_g	Grid inductance	0.36 mH
V_g	Grid voltage	400 V
V_{dc}	DC-link voltage	700 V
f_s	switching frequency	10 kHz

Table (I): system parameters.

Fig. 5: (a): The estimated inductance. $R_g = 0.113$ Ω for t < 0.1 s and $R_g = 0.5$ Ω for t ≥ 0.1 s. (b): Zoom in shows estimation idle instants.

Figure 5 shows the simulation results for system inductance estimation with different grid impedance parameters. The grid resistance is changed at t = 0.1 s from 0.113 Ω to 0.5 Ω and the grid inductance is increased at t = 0.2 s from 0.36 mH to 2 mH. The results show accurate estimation of the change in

grid inductance with insensitivity to resistance variations. The ramp in the estimated inductance is due to the rate limit applied to reduce the effect of noise and measurement filtering. Fig. 5-b shows the instants at which the inductance estimation is disabled to avoid the switching instant ringing/oscillation.

Islanding detection test
One important application of the grid inductance estimation is islanding detection. A simulation scenario for the use of inductance estimator for islanding detection is given in Fig. 6 and the results are shown in Fig. 7.
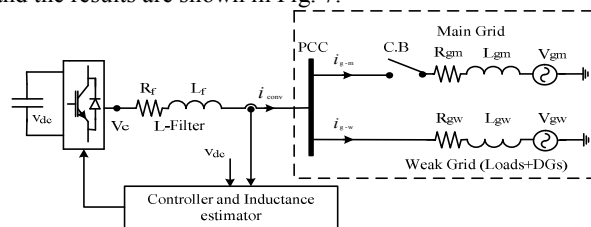

Fig. 6: Islanding test system configuration.

The converter is connected to a grid made up of two connections; one is strong and the other is weak. The strong connection in Fig. 6 is disconnected at t = 0.1 s and the estimated inductance changes to a higher value (see Fig. 7-d) within 50 ms – two supply periods. This is fast enough for the change in the estimated inductance to be used as a flag for islanding.
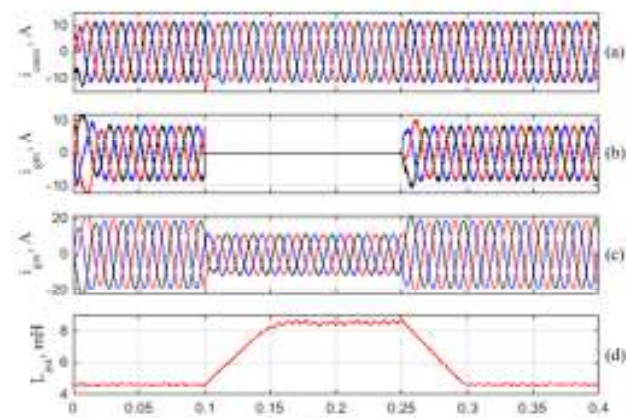

Fig. 7: Simulation results for islanding detection.

Adaptive current control
In this section, the estimated inductance is used for online current control loop adaptation. The simplified block diagram of the current control loop is shown in Fig. 8 and the closed loop transfer function is given by (17).
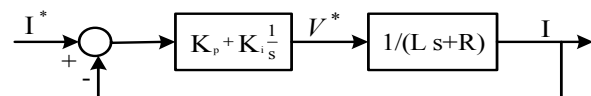

Fig. 8: Simplified block diagram of the current control loop.

$$C(s) = \frac{I(s)}{I^*(s)} = \frac{\frac{1}{L}(K_I + K_P s)}{s^2 + \frac{1}{L}(R + K_P)s + \frac{K_I}{L}} \tag{17}$$

The second order system given by the closed loop transfer function has undamped natural frequency of $\omega_n = \sqrt{K_I/L}$ and damping ratio of $\xi = 0.5\sqrt{\frac{1}{K_I.L}}(R + K_p)$. The controller parameters K_p and K_I are adaptively calculated to achieve a specific bandwidth and damping ratio based on the estimated inductance. The magnitude of the closed loop transfer function $|C(j\omega_{bw})|$ is set to be -3dB at the required bandwidth and damping ratio as given by (18, 19).

$$|C(j\omega_{bw})| = \frac{\left(\frac{\omega_{bw}\,K_p}{L}\right)^2 + \left(\frac{R + K_p}{2L\xi}\right)^4}{(\omega_{bw})^2\left(\frac{R + K_p}{L}\right)^2 + \left[\left(\frac{R + K_p}{2L\xi}\right)^2 - (\omega_{bw})^2\right]^2} = \frac{1}{\sqrt{2}} \quad (18)$$

$$K_i = \frac{1}{L}\left(\frac{R + K_p}{2\xi}\right)^2 \quad (19)$$

Equation (18) is solved using the Newton-Raphson iterative method for K_p and then K_I is calculated using (19) to achieve a bandwidth of 200 Hz and damping ratio of 0.8. The adaptive parameters are updated once every sampling period and the same PI parameters are used for both the d and q current loops.

The adaptation of the PI parameters due to change of the grid inductance is presented in Fig. 9. It can be seen that, at t = 0.05 s the grid inductance is increased to 2 mH giving a total inductance of 6.3 mH. During the change of the estimated inductance the PI parameters are also adapted to achieve the specified bandwidth and damping ratio. Once the new inductance is estimated and becomes constant, the PI parameters also become steadily.
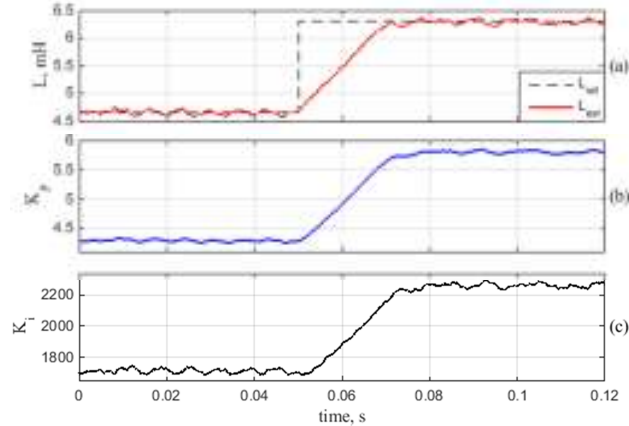

Fig. 9: Adaptation of PI parameter with grid inductance variation.

The time step response at different grid inductance values without and with the adaptive PI controller for d-axis control loop is presented in Fig. 10.

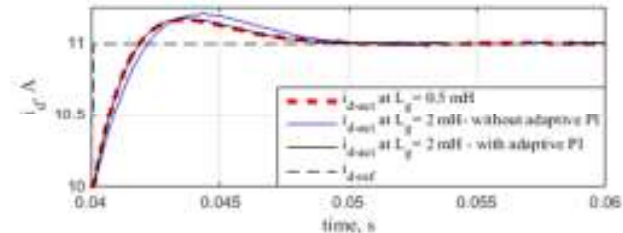

Fig. 10: d-axis step response.

Obviously, it can be seen that without the PI parameter adaptation, an increase in the grid inductance affects the performance of the controller and decreases its bandwidth. In contrast, with the adaptive PI controller, the same step response before and after the grid impedance change is achieved.

V. Experimental Results

To validate the proposed impedance estimator, the current and voltage waveforms of a three-phase grid connected converter were captured and processed. The converter was connected to a Programmable Voltage Source (PVS) via a L-filter and controlled in rectifier mode using Texas Instruments TMS320C6713 DSK fitted with the Actel FPGA A3P400 based board. The output line voltage of the PVS was adjusted at 125 V, the dc-side was set at 200 V and a switching frequency of 1 kHz was used (the switching frequency is low as the rig is part of another project investigating medium voltage switching circuits). The three-phase currents and three PWM line-to-line voltages were captured and stored for 2.5 cycles using two synchronized LeCroy oscilloscopes. The current and voltage signals were sampled at 5 MHz and 50 MHz respectively. The three-phase line-to-neutral voltages were extracted from the measured three-phase line-to-line voltage as:

$$v_{aN} = \frac{1}{3}(v_{ab} - v_{ca}), v_{bN} = \frac{1}{3}(v_{bc} - v_{ab}), v_{cN} = \frac{1}{3}(v_{ca} - v_{bc})(20)$$

One cycle of measured three-phase currents at the input of the converter and the extracted three-phase line-to-neutral voltages are given in Fig. 11.
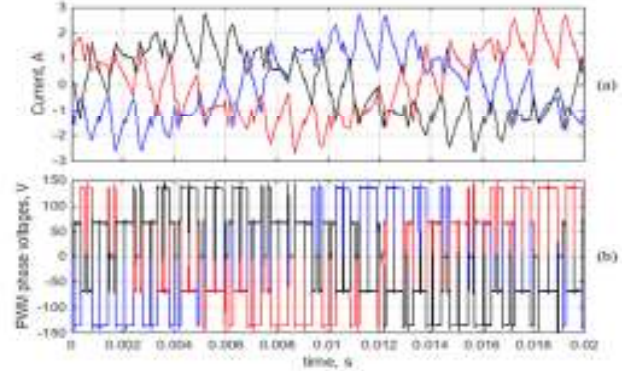

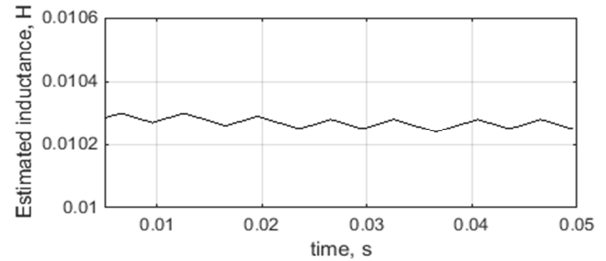Fig. 11: (a): Three-phase supply currents. (b): Three-phase line-to-neutral voltages.

Fig. 12: Estimated inductance.

The current and phase voltage measurements were processed offline using the inductance estimator model given in (15) and the estimated inductance result is shown in Fig. 12. It can

be seen that the average value of the estimated inductance is 10.3 mH. An FFT was applied to the measured current and phase voltage and the inductance was calculated using the switching frequency sideband frequencies as 10.6 mH which is closed to the estimated value, demonstrating the effectiveness of the proposed impedance estimator.

VI.   Conclusion

In this paper, closed form grid inductance and resistance estimation models were derived from the discrete grid connected converter model in the *dq* reference frame. The estimators use two consecutive current samples measured within the SVPWM switching period. The derived inductance and resistance estimator models are fully decoupled and independent. The effectiveness of the proposed estimation approach for islanding detection and adaptive tune (online) of the PI current controller gains are verified by simulation. Experimental results demonstrate the effectiveness of the proposed impedance estimator.

Acknowledgements

References

[1]   T. Strasser, F. Andrén, J. Kathan, C. Cecati, C. Buccella, P. Siano, P. Leitão, G. Zhabelova, V. Vyatkin, P. Vrba, and V. Maˇrík, "A review of architectures and concepts for intelligence in future electric energy systems," *IEEE Trans. Ind. Electron.*, Vol. 62, no. 4, pp. 2424 - 2438, Apr. 2015.

[2]   X. Guo, X. Zhang, B. Wang, W. Wu, and J. M. Guerrero, "Asymmetrical grid fault ride-through strategy of three-phase grid-connected inverter considering network impedance impact in low-voltage grid," *IEEE Trans. Power Electron.*, vol. 29, no. 3, pp. 1064–1068, Mar. 2014.

[3]   M. Sumner, A. Abusorrah, D. Thomas, P. Zanchetta, "Real Time Parameter Estimation for Power Quality Control and Intelligent Protection of Grid-Connected Power Electronic Converters," *IEEE Trans. Smart grid*, Vol. 5, no. 4, pp. 1602 – 1607, Jul. 2014.

[4]   M. Ciobotaru, R. Teodorescu, P. Rodriguez, A. Timbus, and F. Blaabjerg, "Online grid impedance estimation for single-phase grid-connected systems using PQ variations," in *Proc. 38th IEEE Power Electronics Specialists Conf. (PESC)*, pp. 2306–2312, Jun. 2007.

[5]   B. Palethorpe, M. Sumner, and D. Thomas, "Power system impedance measurement using a power electronic converter," in *Proc. of Harmonics and Quality of Power*, vol. 1, pp. 208–213, 2000.

[6]   M. Cespedes and J. Sun, "Online grid impedance identification for adaptive control of grid-connected inverters," in *Proc. IEEE ECCE, Raleigh, NC, USA*, pp. 914–921, 2012.

[7]   M. Sumner, D.W.P Thomas, A. Abusorrah, and P. Zanchetta, "Power System Impedance Estimation for Improved Active Filter Control, using Continuous Wavelet Transforms," *Proc. IEEE Power Eng. Soc. Transmission Distribution Conf. Exhibit.*, pp.653-658, May 21-24, 2006.

[8]   L. Asiminoaei , R. Teodorescu , F. Blaabjerg and U. Borup "Implementation and test of an online embedded grid impedance estimation technique for PV inverters, " *IEEE Trans. Ind. Electron.*, vol. 52, no. 4, pp.1136 -1144, 2005.

[9]   M. Ciobotaru, R. Teodorescu, and F. Blaabjerg, "On-line grid impedance estimation based on harmonic injection for grid-connected PV inverter," in *Proc. IEEE ISIE*,, pp. 2437–2442, Jun. 2007.

[10]   S. Neshvad, S. Chatzinotas, J. Sachau, "Wideband Identification of Power Network Parameters Using Pseudo-Random Binary Sequences on Power Inverters," *IEEE Trans. Smart grid*, vol. 6, no. 5, pp. 2293–2301, Sep. 2015.

[11]   H. Gu, X. Guo, D. Wang, and W. Wu, "Real-time Grid Impedance Estimation Technique for Grid-Connected Power Converters, " *IEEE International Symposium on Industrial Electronics (ISlE)*, pp. 1621- 1626, Hangzhou, 28-31 May 2012.

[12]   M. Liserre, F. Blaabjerg and R. Teodorescu, "Grid Impedance Estimation via Excitation of LCL-Filter Resonance," *IEEE Trans. on Industry Applications*, vol. 43, pp. 1401–1407, Sep. 2007.

[13]   N. Hoffmann and F. W. Fuchs, "Minimal invasive equivalent grid impedance estimation in inductive-resistive power-networks using extended Kalman-filter," *IEEE Trans. Power Electron.*, vol. 29, no. 2, pp. 631–641, Feb. 2014.

[14]   B. Arif, L. Tarisciotti, P. Zanchetta, J. Clare, "Grid parameter estimation using model predictive direct power control, " *IEEE Trans. on Industry Applications*, vol. 51, pp. 4614–4622, Nov. 2015.

[15]   J.Z. Zhou, Hui Ding, Shengtao Fan, Yi Zhang, A.M. Gole, "Impact of Short-Circuit Ratio and Phase-Locked-Loop Parameters on the Small-Signal Behavior of a VSC-HVDC Converter , " *Power Delivery, IEEE Transactions on*, vol. 29, no. 5, pp. 2287-2296 , Oct. 2014.

[16]   D. Li, Y. Notohara, Y. Iwaji, Y. Kurita, "AC voltage and current sensorless control method for three-phase PWM converter, " *Wiley Periodicals, Inc. Electrical Engineering in Japan*, vol. 172, no. 4, pp. 48–57, Sep. 2010.

[17]   Z. Shu, J. Tang, and J. Lian, "An efficient SVPWM algorithm with low computational overhead for three phase inverters," *IEEE Trans. Power Electron.*, vol. 22, no. 5, pp. 1797–1805, Sep. 2007.

[18]   A. E. Ginart, D. W. Brown, P. W. Kalgren, and M. J. Roemer, "Online ringing characterization as a diagnostic technique for IGBTs in power drives," *IEEE Trans. Instrum. Meas.*, vol. 58, no. 7, pp. 2290–2299, Jul. 2009.